Published in final edited form as:
Ann Biomed Eng. 2020 August ; 48(8): 2268–2278. doi:10.1007/s10439-020-02500-5.

Targeted Gold Nanoparticles as an Indicator of Mechanical Damage in an Elastase Model of Aortic Aneurysm

Brooks A. Lane[1], **Xiaoying Wang**[2], **Susan M. Lessner**[1,3], **Naren R. Vyavahare**[2], **John F. Eberth**[1,3]

[1]Biomedical Engineering Program, University of South Carolina, Columbia, SC 29208, USA;

[2]Bioengineering Department, Clemson University, Clemson, SC, USA;

[3]Cell Biology and Anatomy Department, University of South Carolina, Columbia, SC, USA

Abstract

Elastin is a key structural protein and its pathological degradation deterministic in aortic aneurysm (AA) outcomes. Unfortunately, using current diagnostic and clinical surveillance techniques the integrity of the elastic fiber network can only be assessed invasively. To address this, we employed fragmented elastin-targeting gold nanoparticles (EL-AuNPs) as a diagnostic tool for the evaluation of unruptured AAs. Electron dense EL-AuNPs were visualized within AAs using micro-computed tomography (micro-CT) and the corresponding Gold-to-Tissue volume ratios quantified. The Gold-to-Tissue volume ratios correlated strongly with the concentration (0, 0.5, or 10 U/mL) of infused porcine pancreatic elastase and therefore the degree of elastin damage. Hyperspectral mapping confirmed the spatial targeting of the EL-AuNPs to the sites of damaged elastin. Nonparametric Spearman's rank correlation indicated that the micro-CT-based Gold-to-Tissue volume ratios had a strong correlation with loaded ($\rho = 0.867$, p-val = 0.015) and unloaded ($\rho = 0.830$, p-val = 0.005) vessel diameter, percent dilation ($\rho = 0.976$, p-val = 0.015), circumferential stress ($\rho = 0.673$, p-val = 0.007), loaded ($\rho = -0.673$, p-val = 0.017) and unloaded ($\rho = -0.697$, p-val = 0.031) wall thicknesses, circumferential stretch ($\rho = -0.7234$, p-val = 0.018), and lumen area compliance ($\rho = -0.831$, p-val = 0.003). Likewise, in terms of axial force and axial stress vs. stretch, the post-elastase vessels were stiffer. Collectively, these findings suggest that, when combined with CT imaging, EL-AuNPs can be used as a powerful tool in the non-destructive estimation of mechanical and geometric features of AAs.

Keywords

Aortic aneurysm; Cardiovascular biomechanics; Computed tomography; Gold nanoparticles; Elastin degradation

---

Address correspondence to John F. Eberth, Biomedical Engineering Program, University of South Carolina, Columbia, SC 29208, USA. john.eberth@uscmed.sc.edu.

CONFLICT OF INTEREST
NRV has equity in Elastrin Therapeutics Inc. which has licensed this technology from Clemson University. Otherwise, no benefits have been or will be received from a commercial party related directly or indirectly to this manuscript.

INTRODUCTION

Aortic aneurysms (AAs) are a complex form of aortopathy described as a focal dilation of the vascular wall exceeding 1.5-times the normal vessel diameter.[2,11] Many AAs are asymptomatic, and those that are identified often have large disparities in clinical outcomes ranging from stabilization to rupture.[20,24] Although diameter and growth rate are two important factors in the evaluation of potential clinical outcomes, biomechanical properties and microstructural integrity have important impacts on disease morbidity and mortality.[9,21,28,41] Other pathological hallmarks of AAs include inflammation, atherosclerosis, wall thinning, vascular stiffening, dissection, and dysfunctional mechanosensing.[35] These factors are accompanied by comorbidities including myocardial infarction, claudication and stroke.[25] Thus, while rupture is an important and decisive end-point in the progression of aneurysmal disease, the altered mechanical properties of intact AAs should not be overlooked. Since there are currently no approved therapeutic management strategies for mitigation of AAs, options are limited to open surgical or endovascular repair with astonishingly high perioperative mortality rates.[2,6,19] Overall, there exists a tremendous need for improved methods of predicting, diagnosing, and evaluating AAs that can be utilized for patient-specific care strategies.

AAs are intimately associated with extracellular matrix (ECM) proteolysis and inflammation.[3,18,31,36,40] Elastin, a component of the ECM, is essential to the structural integrity of large arteries and conditions that compromise elastic fiber structure and function result in diverse aortopathies.[10,17,26,34] Likewise, inflammatory cells and dysfunctional smooth muscle cells overexpressing matrix metalloproteases (MMPs) lead to unbalanced collagen turnover and extensive elastin fragmentation and elastolysis.[4,7,8,14,37,38] The resulting elastin fragments are known pro-inflammatory chemoattractants and elicit compounded immune responses causing a vicious cycle of AA progression.[1] Considering both its structural and signaling roles in disease progression, it is plausible that tracking alterations in the structural integrity of elastin could aid in AA diagnosis and surveillance and may even be used to predict AA formation. Thus, a non-invasive diagnostic tool that provides visualization of local elastolysis can enable clinicians to better evaluate AAs.[22]

To that end, we have adapted injectable gold nanoparticles conjugated to an antibody against fragmented elastin (EL-AuNP).[42] EL-AuNP-laden AAs are readily imaged through the use of computed tomography (CT) due to gold’s high electron density.[27,30,39] Previous research by our group using a low-density lipoprotein receptor knockout and angiotensin-II infusion model revealed that systemic administration of these fragmented elastin-targeting EL-AuNPs in mice resulted in localization of the EL-AuNPs to the aneurysmal site in an amount that correlated strongly with tissue failure.[42] That work demonstrated the tremendous utility of EL-AuNPs with CT imaging as a diagnostic tool. Nevertheless, AAs have diverse etiologies and the current study utilizes an alternate approach to AA formation through protease administration. Furthermore, this manuscript focuses on non-destructive mechanical properties that likely play a broader role in long-term cardiovascular health. Here porcine pancreatic elastase infusion is performed on murine infrarenal aortas to generate a significant but uniform dilation *in vitro*. Due to the resultant axial symmetry, these AAs are well suited to conventional biaxial analyses.[10,17] We then use micro-CT to investigate the uptake of fragmented EL-AuNPs using arteries exposed to three concentrations of elastase (0, 0.5, 10 U/mL), each generating different degrees of elastolysis, and utilize standard biaxial mechanical analyses to determine the relationship between EL-AuNP uptake and arterial mechanics. As confirmation of elastin damage and EL-AuNP targeting, EL-AuNPs are spatially mapped within the vascular wall using hyperspectral mapping.

MATERIALS AND METHODS

Specimen Preparation

All animal protocols were approved through the Institutional Animal Care and Use Committee at the University of South Carolina. Wild-type 12-week-old C57BL/6J (JAX #000664) male mice ($n = 13$) were euthanized *via* carbon dioxide inhalation and perfused *via* left ventricle puncture with saline solution supplemented with 30 U/mL sodium heparin at 100 mmHg. The abdominal aorta was isolated from the iliac bifurcation to the left renal artery *via* careful dissection from the surrounding perivascular tissues. Branches were carefully ligated using 10/0 nylon suture and the infrarenal aorta was cannulated on blunted 26G needles. Vessels were placed in a solution of phosphate-buffered saline (PBS) prior to mechanical testing which typically occurred about 3 h after animal sacrifice.

Biaxial Mechanical Testing and Data Analysis

The infrarenal aortas were mounted within our custom-designed biaxial testing rig equipped with a thin load-beam cell (LCL-113G; Omega Engineering), pressure transducer (PX409; Omega Engineering), syringe pump (AL-1000; World Precision Instruments), and motorized axial actuator (Z825B; Thorlabs). All components are computer-controlled and measurements are synchronized *via* a custom LabView code. The testing chamber was filled with a PBS solution, and PBS was flushed through the vessel lumen and device tubing to remove bubbles and to maintain tissue hydration throughout testing. The artery then underwent five axial preconditioning cycles from the unloaded length to 10% above the estimated *in vivo* stretch ratio (0 to 20–50 mN) followed by five cyclic pressurizations from 10 to 160 mmHg at the *in vivo* axial stretch ratio. The *in vivo* axial stretch ratio was estimated through a series of axia force-extension tests at fixed luminal pressures to identify the force-pressure invariant relationship.[15]

For data acquisition, the artery was extended to three axial stretch ratios (*in vivo* ± 10%) before undergoing three pressurization cycles (0–160 mmHg) with simultaneous force and outer diameter measurements at 10 mmHg pressure increments. Due to the semi-transparency of the vascular wall and the assumption of axial symmetry, inner diameters were also recorded in real-time. The elastase treatment groups first underwent these mechanical testing protocols. Then the aorta was perfused intraluminally with 0.5 ($n = 4$) or 10 U/mL ($n = 5$) porcine pancreatic elastase solution and subsequently pressurized to 100 mmHg for 30 min at the *in vivo* stretch ratio. This step was followed by perfusion with Halt protease inhibitor cocktail containing aprotinin, a known serine protease inhibitor. The new unloaded geometry was recorded and vessels subsequently underwent the same testing protocols described above at a common axial stretch ratio of 1.2. Elastase-treated tissues were tested to 140 mmHg to limit premature failure.

The mean circumferential and axial Cauchy stresses are calculated from

$$\sigma_\theta = \frac{Pr_i}{h}, \quad \sigma_z = \frac{f}{\pi\left(r_0^2 - r_i^2\right)}, \tag{1}$$

where r_i and r_0 are the deformed inner and outer radii, P the transmural pressure, f the axial force, and h the deformed wall thickness.

Likewise, the mid-wall circumferential and axial stretch ratios are calculated from

$$\lambda_\theta = \frac{(r_i + r_0)}{(R_i + R_0)}, \quad \lambda_z = \frac{\ell}{L}, \tag{2}$$

where R_i and R_0 are the unloaded radii and ℓ and L the deformed and undeformed vessel lengths, respectively. Using this convention, H (used in Tables 1 and 2) refers to the unloaded wall thickness, while d and D are the loaded and unloaded outer diameters.

Dilation and vessel elongation were then calculated from the ratio of loaded outer diameters and unloaded segment lengths, respectively, before (pre) and after (post) elastase exposure

$$\delta = \frac{d_{\text{post}}}{d_{\text{pre}}}, \quad \Lambda = \frac{L_{\text{post}}}{L_{\text{pre}}}. \tag{3}$$

The lumen area compliance was estimated from

$$c = \pi\frac{\Delta r_i^2}{\Delta P}, \tag{4}$$

where ΔP is the change from diastolic to systolic transmural pressures (80 to 120 mmHg) with corresponding inner radii measurements at these pressures.

Preparation and Use of Antibody-Conjugated Gold Nanoparticles

Fragmented elastin-targeting gold nanoparticles (EL-AuNPs) were synthesized as previously described.[42] Briefly, citrate-capped gold nanoparticles (150 ± 20 nm) underwent PEGylation and conjugation to a custom-made anti-elastin antibody (synthesized in-house at Clemson University) *via* carbodiimide EDC and sulfo-NHS chemistry. Additionally, a separate AuNP solution was prepared in a similar manner but conjugated with a non-reactive IgG antibody (IgG-AuNPs). The excess antibody was removed *via* centrifugation, and nanoparticles were resuspended at a final concentration of 3 mg/mL in PBS. Prior to use in our system, the EL- or IgG-AuNP suspensions were periodically vortexed to create homogeneous solutions.

At the conclusion of mechanical testing, the infrarenal aortas in the 0 U/mL, 0.5 U/mL, and 10 U/mL elastase infused experimental groups were removed from the device and placed in PBS where the branch ligatures were removed to provide the greatest intraluminal access for the AuNPs. The aortas were then placed in the EL-AuNP solution on a shaker plate overnight at 4 °C. Concurrently, an additional 10 U/mL elastase infused aorta was tested and subsequently placed in the non-reactive IgG-AuNP solution. The aortas were removed from the AuNP solutions and placed in PBS for 1 h on a shaker plate to remove excess unbound gold nanoparticles.

Micro-Computed Tomography Imaging

Aortas were immersed in corn oil and imaged (90 kV, 88 mAs, 18 × 18 voxel size, 0.2 mm Cu filter) using a Quantum GX Micro-CT Imaging System (PerkinElmer). All CT scans were visualized and reconstructed using Caliper Analyze software (Analyze Direct, Inc.). Prior to analysis, each scan underwent stoichiometric Hounsfield unit calibration using the air above the sample and the specimen stage to obtain accurate relationships between CT Hounsfield units and electron densities. Aortic tissues and gold nanoparticle signals were segmented separately and analyzed using the Caliper software volume-rendering feature.

Histology

At the conclusion of micro-CT imaging, samples were placed in 4% paraformaldehyde at 4 °C overnight. Samples from each group were then paraffin-embedded and sectioned (5 μm) for Hematoxylin and Eosin (H&E) staining and elastin autofluorescence. Elastin was identified through autofluorescence using 470/22 excitation and 510/42 emission filters. Images were acquired on an EVOS FL Auto 2 microscope. Additional samples were embedded in OCT and cryosectioned (5 μm) to preserve the AuNP signal. These cryosections were examined with a CytoViva enhanced darkfield microscope optics system (CytoViva, Inc., Auburn, AL). The system (Olympus BX51) employs an immersion oil (Type A, nd > 1.515, Cargille Brand) ultra-dark-field condenser and a 100 × oil immersion objective with an adjustable numerical aperture from 1.2 to 1.4. Illumination was provided by a Fiber-lite DC 950 regulated illuminator. Enhanced darkfield microscopy (EDFM) images were obtained using Exponent7 software with a gain setting of 2.8 and an exposure time of 435 ms to visualize the EL-AuNPs. A hyperspectral imager (HSI) (mounted on a microscope and controlled by Environment for Visualization software from Exelis Visual Information Solutions, Inc.) was used to extract spectral information for mapping the AuNPs in the samples at an exposure time of 0.25 ms with a full field of view (730 lines). Negative control samples (without AuNPs) were imaged and analyzed to create a spectral library as a reference. Gold mapping was achieved by applying a filtered spectral library by subtracting the negative control spectral library. The auto-fluorescence of the elastin was captured in combination with their transmitted light image to visualize the spatial distribution of the elastin within the tissue.

Statistics and Regression Analysis

Graphical results of mechanical data are presented as the mean ± standard deviation. The non-parametric analysis for calculating Spearman's Rho correlation coefficients ρ [1,− 1] was performed to evaluate the strength of monotonic relationships between material/geometrical parameters and Gold-to-Tissue volume ratios with values of 1, 0 and − 1 indicating strong positive, zero, or strong negative associations between parameters, respectively. Significant relationships were plotted with Ordinary Least Squares (OLS) regressions. One-way ANOVA analysis was performed on micro-CT results and parameter comparisons between groups, with (*) and (**) denoting statistical differences between controls and 0.5 U/mL or 10 U/mL at p-val < 0.05 and p-val < 0.1, respectively, while (^) denotes differences between 0.5 U/mL and 10 U/mL experimental groups at p-val < 0.05.

RESULTS

Intraluminal elastase exposure at 100 mmHg for 30 min followed by perfusion of a protease inhibitor generated progressive but consistent dilation across all specimens (0.5 U/mL = 12.0 ± 3.0%, 10 U/mL = 24.0 ± 1.0%; p-val < 0.001) (Fig. 1; Table 1). Dilation was below the clinically designated threshold of 1.5-times the normal diameter and was thus comparable to developing aneurysms or pre-aneurysmal vessels. Vessel undeformed lengths also increased with increasing elastase concentrations (0.5 U/mL = 1.59 ± 0.05%, 10 U/mL = 1.66 ± 0.07%), although not significantly different between elastase concentration groups (p-val = 0.13). Regardless, all vessels reported here were stable and held pressure before and after elastase exposure. A small group ($n = 2$) of elastase-exposed arteries failed at the ligation point due to changes in wall thickness and were discarded. All discrete data with statistical significance are reported in Table 1.

A rightward shift in the pressure-diameter curves indicated increased dilation with elastase concentration across the entire pressure range with a diminished inflection point normally observed in elastic arteries of small animals (Fig. 2a). Accordingly, both unloaded (p-val = 0.079) and physiologically loaded (p-val = 0.032) outer diameters significantly increased with elastase concentration while unloaded (p-val = 0.023) and loaded (p-val = 0.026) wall thicknesses were only found to be significantly decreased between the 0 U/mL controls and the 0.5 U/mL or 10 U/mL experimental groups. Force invariant pressurization behavior was observed in 0 U/mL controls at an axial stretch ratio of 1.61 ± 0.03. However, direct observation of the axial-force vs. pressure relationship showed an increasing value of axial force for 0.5 U/mL and 10 U/mL experimental groups compared to the force-invariant pressure relationship of the controls (Fig. 2b), even at an axial stretch ratio of 1.2, well below the pre-elastase *in vivo* axial stretch ratio of the controls. Accordingly, a significantly higher force was recorded for physiological pressures at these axial stretch ratios for the 10 U/mL group compared to 0 U/mL controls (p-val = 0.040) or 0.5 U/mL experimental groups (p-val < 0.001). Overall, the axial force was much higher in the experimental elastase groups for a comparable axial stretch.

A decrease in lumen area compliance was present in all elastase treatment groups, only reaching statistical significance for the 10 U/mL group compared to 0 U/mL controls (p-val = 0.042) (Table 1). A gradual increase in stiffness was observed in the circumferential direction as indicated by the slope of the stretch-stress responses (Fig. 2c). At physiological conditions, this stiffness increase corresponded to lower circumferential stretches between 0 U/mL controls and 0.5 U/mL (p-val = 0.017) and 10 U/mL (p-val < 0.001) experimental groups as well as between the 0.5 U/mL and 10 U/mL groups (p-val < 0.001). Lower circumferential stretches were associated with higher circumferential stresses between 0 U/mL controls and 0.5 U/mL (p-val = 0.022) and 10 U/mL (p-val = 0.001) experimental groups, as well as between the 0.5 U/mL and 10 U/mL groups (p-val = 0.025). Although experimental elastase-treated vessels were referenced at a lower axial stretch ratio, the axial stresses trended higher in the 0.5 U/mL group and were significantly higher in the 10 U/mL (p-val = 0.074) experimental group (Table 1). Therefore, elastase treatment caused increased axial stiffening.

Considerable fragmentation of the elastic lamellae was evident in the microstructure, especially at higher elastase concentrations (Figs. 3e and 3f). Micro-CT results confirmed the elastin fragmentation through increases in localization of EL-AuNPs within tissues exposed to 0.5 U/mL and 10 U/mL elastase when compared to 0 U/mL controls (Fig. 4). Of note, some EL-AuNPs accumulated near the severed ends of the 0 U/mL control arteries and along the ligated branches, likely due to surgical damage introduced at those locations during specimen preparation. Thorough washing did not remove these particles that were firmly adhered to the matrix. Overall, the Gold-to-Tissue volume ratios increased along with elastase concentrations (0 U/mL = 0.37 ± 0.3%; 0.5 U/mL = 4.70 ± 2.2%; 10 U/mL = 7.56 ± 2.0%) with statistical significance between all groups (Fig. 5). Further histological examination using elastin autofluorescence, EDFM, HSI, and spectral mapping (Figs. 6a–6d, 1–3) supported micro-CT results with increasing EL-AuNP localization and uptake mostly localized to the medial section of the damaged tissues. Additionally, the 10 U/mL elastase infused aorta incubated with the non-reactive IgG-AuNP (Figs. 6a–6d, 4) showed a large degree of elastolysis but no AuNP signal mapped from EDFM and HSI.

Spearman's Rho coefficients showed significant positive associations between Gold-to-Tissue volume ratios and dilation percentage ($\rho = 0.976$), loaded and unloaded outer diameter ($\rho = 0.867$, $\rho = 0.830$), and circumferential stresses ($\rho = 0.673$), whereas loaded and unloaded thicknesses ($\rho = -0.673$, $\rho = -0.697$), circumferential stretch ratio ($\rho = -0.723$), and lumen area compliance ($\rho = -0.831$) had negative but significant associations (Table 2). Axial undeformed elongation, stress, and force were not found to correlate with the Gold-to-Tissue ratio; however, it is important to note that the force and stress values were not recorded at a common axial stretch ratio due to the dramatic increase in axial stiffness. OLS regressions of significant variables measured under physiological conditions are shown in Fig. 7 and regression statistics evaluating the strength of the linear relationship between the two variables can be found in Table 2. The dilation percentage regression exhibited the greatest R^2 value (0.92), indicating a strong linear relationship while the circumferential stretch had the lowest R^2 value (0.51) indicating a poorer linear fit.

DISCUSSION

AA models present with diverse and varying biomechanical phenotypes.[13,16] The elastase infusion model, for example, has been used in prior work to eliminate elastin function within the artery to mimic extreme aneurysm phenotypes.[5,10,43] In this work, however, we perfused at both low and high elastase concentrations to induce a moderate aneurysm phenotype below the 1.5-fold clinical threshold.[2,11] These pre- and small aneurysmal vessels were compared to 0 U/mL controls, and each group of vessels was exposed intraluminally to EL-AuNPs to identify progressive gold accumulation in damaged tissue. Interestingly, EL-AuNP binding also occurred in the control vessels at locations where elastin damage occurred due to cutting or ligation. Furthermore, even after large elastolysis, treatment with a non-reactive IgG-AuNP showed no localization within the arterial tissue indicating that potential changes in tissue porosity due to elastase exposure did not lead to AuNP sequestration and suggest effective elastin fragment targeting using the EL-AuNPs. This deposition is fortuitous, suggesting a potential post-surgical role for this technology to assess surgical damage to the underlying microstructure.

Medial thinning and a gradual loss of elastin after elastase perfusion resulted in biaxial mechanical changes reflected in the observed dilation, gradual increases in axial and circumferential stresses, and an overall arterial stiffening with increasing elastase concentrations. These changes recapitulate observations of increased vascular stiffening in the pathological progression of AAs.[23,33] Although the model is greatly simplified, the resulting varied degree of elastolysis proves useful for *in vitro* analyses and quantification of mechanical properties in transient stages of AA disease in a configuration that is measurable using standard biaxial techniques.[10,17] By comparison, *in vivo* analysis of vascular mechanics is limited. For example, the increased axial stiffening observed here can only be measured *in vitro*. Thus, the current work was used to motivate the use of elastin fragment-targeting EL-AuNPs as a diagnostic tool. This *in vitro* analysis also readily illustrates the effects of increasing the collagen-to-elastin ratio (here through elastolysis) with a diminished low-pressure inflection pattern. This inflection is normally observed in small rodent elastic arteries that possess a low collagen-to-elastin ratio.[12,32]

As espoused above, temporal progression and severity of AA disease can be reflected in deviations from the native homeostatic mechanical environment leading to maladaptive remodeling processes that further exacerbate disease progression. However, the current clinical approach to evaluate aneurysm stability is limited to macroscopic assessments that lack direct interpretation of mechanical properties.[29] To build upon previous research revealing a correlation between elastin fragment-targeting EL-AuNPs and tissue failure,[42] here we show that in two different severities of aneurysmal disease, the EL-AuNP binding is linked to non-destructive descriptors of arterial mechanics. The non-parametric Spearman's rank coefficient indicated that a greater uptake of EL-AuNPs (*via* Gold-to-Tissue volume ratio) is strongly associated with increased dilation, larger outer diameters, and increased circumferential stresses when measured at common loading conditions. Furthermore, increased EL-AuNP binding was strongly associated with decreased medial thickness, diameter distensibility, and lumen area compliance. Decreased thickness is a direct result of elastolysis in our model but is normally attributed to broad proteolysis or apoptosis found in chronic *in vivo* models.[31] Although we are hesitant to assume a linear model, linear regression analyses revealed significant relationships between EL-AuNP uptake and material descriptors, thereby further supporting links between EL-AuNP localization and arterial mechanics.

Elastin degradation is a key manifestation of AAs ultimately affecting the stability and function of the vessel wall. Identifying the relationships between binding of a fragmented elastin-targeting EL-AuNP and local arterial mechanics enables clinicians to gather local histomechanical information directly linked to AA stability through routinely used CT imaging techniques. Paired with previous diagnostic and clinical indices, patient-specific care and intervention strategies can be refined to prevent unnecessary interventions or to advocate for prompt intervention prior to meeting established interventional criteria.

ACKNOWLEDGMENTS

The authors would like to acknowledge Lorain Junor and Nazli Gharraee for their assistance in micro-CT training and analysis. This work was supported by the National Institutes of Health under Grant Numbers (R01HL133662 and R01HL145064) and in part by the National Science Foundation under Grant Number CMMI-1760906.

REFERENCES

1. Adair-Kirk T, and Senior R. Fragments of extracellular matrix as mediators of inflammation. Int. J. Biochem. Cell Biol 40:1101–1110, 2008. [PubMed: 18243041]
2. Aggarwal S, Qamar A, Sharma V, and Sharma A. Abdominal aortic aneurysm: a comprehensive review. Exp. Clin. Cardiol 16:11–15, 2011. [PubMed: 21523201]
3. Ailawadi G, Eliason JL, and Upchurch GR. Current concepts in the pathogenesis of abdominal aortic aneurysm. J. Vasc. Surg 38:584–588, 2003. [PubMed: 12947280]
4. Airhart N, Brownstein BH, Cobb JP, Schierding W, Arif B, Ennis TL, Thompson RW, and Curci JA. Smooth muscle cells from abdominal aortic aneurysms are unique and can independently and synergistically degrade insoluble elastin. J. Vasc. Surg 60:1033–1042.e5, 2014. [PubMed: 24080131]
5. Azuma J, Asagami T, Dalman R, and Tsao PS. Creation of murine experimental abdominal aortic aneurysms with elastase. J. Vis. Exp 29:e1280, 2009.
6. Baxter BT, Terrin MC, and Dalman RL. Medical management of small abdominal aortic aneurysms. Circulation 117:1883–1889, 2008. [PubMed: 18391122]
7. Campa JS, Greenhalgh RM, and Powell JT. Elastin degradation in abdominal aortic aneurysms. Atherosclerosis 65:13–21, 1987. [PubMed: 3649236]
8. Carmo M, Colombo L, Bruno A, Corsi FRM, Roncoroni L, Cuttin MS, Radice F, Mussini E, and Settembrini PG. Alteration of elastin, collagen and their cross-links in abdominal aortic aneurysms. Eur. J. Vasc. Endovasc. Surg 23:543–549, 2002. [PubMed: 12093072]
9. Choksy SA, Wilmink AB, and Quick CR. Ruptured abdominal aortic aneurysm in the Huntingdon district: a 10-year experience. Ann. R. Coll. Surg. Engl 81:27–31, 1999. [PubMed: 10325681]
10. Collins MJ, Eberth JF, Wilson E, and Humphrey JD. Acute mechanical effects of elastase on the infrarenal mouse aorta: implications for models of aneurysms. J. Biomech 45:660–665, 2012. [PubMed: 22236532]
11. Cooper MA, and Upchurch GR Jr. The society of vascular surgery practice guidelines on the care of patients with abdominal aortic aneurysms. JAMA Surg. 154:553–554, 2019. [PubMed: 30994867]
12. Cox RH Comparison of carotid artery mechanisms in the rat, rabbit, and dog. Am. J. Physiol 234:H280, 1978. [PubMed: 629363]
13. Daugherty A, and Cassis LA. Mouse models of abdominal aortic aneurysms. Arterioscler. Thromb. Vasc. Biol 24:429–434, 2004. [PubMed: 14739119]
14. Dobrin PB, and Mrkvicka R. Failure of elastin or collagen as possible critical connective tissue alterations underlying aneurysmal dilatation. Vascular 2:484–488, 1994.
15. Eberth JF, Taucer AI, Wilson E, and Humphrey JD. Mechanics of carotid arteries in a mouse model of marfan syndrome. Ann. Biomed. Eng 37:1093–1104, 2009. [PubMed: 19350391]
16. Ferruzzi J, Bersi MR, and Humphrey JD. Biomechanical phenotyping of central arteries in health and disease: advantages of and methods for murine models. Ann. Biomed. Eng 41:1311–1330, 2013. [PubMed: 23549898]
17. Ferruzzi J, Collins MJ, Yeh AT, and Humphrey JD. Mechanical assessment of elastin integrity in fibrillin-1-deficient carotid arteries: implications for Marfan syndrome. Cardiovasc. Res 92:287–295, 2011. [PubMed: 21730037]

18. Fillinger MF, Raghavan ML, Marra SP, Cronenwett JL, and Kennedy FE. In vivo analysis of mechanical wall stress and abdominal aortic aneurysm rupture risk. J. Vasc. Surg 36:589–597, 2002. [PubMed: 12218986]
19. Gazoni LM, Speir AM, Kron IL, Fonner E, and Crosby IK. Elective thoracic aortic aneurysm surgery: better outcomes from high-volume centers. J. Am. Coll. Surg 210:855–859, 2010. [PubMed: 20421065]
20. Grant MW, Thomson IA, and van Rij AM. In-hospital mortality of ruptured abdominal aortic aneurysm. ANZ J. Surg 78:698–704, 2008. [PubMed: 18796032]
21. Hall AJ, Busse EFG, McCarville DJ, and Burgess JJ. Aortic wall tension as a predictive factor for abdominal aortic aneurysm rupture: improving the selection of patients for abdominal aortic aneurysm repair. Ann. Vasc. Surg 14:152–157, 2000. [PubMed: 10742430]
22. Holmes DR, Liao S, Parks WC, and Hompson RW. Medial neovascularization in abdominal aortic aneurysms: a histopathologic marker of aneurysmal degeneration with pathophysiologic implications. J. Vasc. Surg 21:761–772, 1995. [PubMed: 7539511]
23. Iliopoulos DC, Kritharis EP, Giagini AT, Papadodima SA, and Sokolis DP. Ascending thoracic aortic aneurysms are associated with compositional remodeling and vessel stiffening but not weakening in age-matched subjects. J. Thorac. Cardiovasc. Surg 137:101–109, 2009. [PubMed: 19154911]
24. Johansson G, Markström U, and Swedenborg J. Ruptured thoracic aortic aneurysms: a study of incidence and mortality rates. J. Vasc. Surg 21:985–988, 1995. [PubMed: 7776479]
25. Kanagasabay R, Gajraj H, Pointon L, and Scott RAP. Co-morbidity in patients with abdominal aortic aneurysm. J. Med. Screen 3:208–210, 1996. [PubMed: 9041487]
26. Lee JS, Basalyga DM, Simionescu A, Isenburg JC, Simionescu DT, and Vyavahare NR. Elastin calcification in the rat subdermal model is accompanied by upregulation of degradative and osteogenic cellular responses. Am. J. Pathol 168:490–498, 2006. [PubMed: 16436663]
27. Lei Y, Nosoudi N, and Vyavahare N. Targeted chelation therapy with EDTA-loaded albumin nanoparticles regresses arterial calcification without causing systemic side effects. J. Control. Release 196:79–86, 2014. [PubMed: 25285609]
28. Maier A, Gee MW, Reeps C, Pongratz J, Eckstein H-H, and Wall WA. A comparison of diameter, wall stress, and rupture potential index for abdominal aortic aneurysm rupture risk prediction. Ann. Biomed. Eng 38:3124–3134, 2010. [PubMed: 20480238]
29. Moxon JV, Parr A, Emeto TI, Walker P, Norman PE, and Golledge J. Diagnosis and monitoring of abdominal aortic aneurysm: current status and future prospects. Curr. Probl. Cardiol 35:512–548, 2010. [PubMed: 20932435]
30. Ostdiek AM, Ivey JR, Grant DA, Gopaldas J, and Grant SA. An in vivo study of a gold nanocomposite biomaterial for vascular repair. Biomaterials 65:175–183, 2015. [PubMed: 26164402]
31. Petersen E, Wågberg F, and Angquist KA. Proteolysis of the abdominal aortic aneurysm wall and the association with rupture. Eur. J. Vasc. Endovasc. Surg 23:153–157, 2002. [PubMed: 11863333]
32. Prim DA, Mohamed MA, Lane BA, Poblete K, Wierzbicki MA, Lessner SM, Shazly T, and Eberth JF. Comparative mechanics of diverse mammalian carotid arteries. PLoS ONE 13:e0202123, 2018. [PubMed: 30096185]
33. Raaz U, Zöllner AM, Schellinger IN, Toh R, Nakagami F, Brandt M, Emrich FC, Kayama Y, Eken S, Adam M, Maegdefessel L, Hertel T, Deng A, Jagger A, Buerke M, Dalman RL, Spin JM, Kuhl E, and Tsao PS. Segmental aortic stiffening contributes to experimental abdominal aortic aneurysm development. Circulation 131:1783–1795, 2015. [PubMed: 25904646]
34. Rezakhaniha R, Fonck E, Genoud C, and Stergiopulos N. Role of elastin anisotropy in structural strain energy functions of arterial tissue. Biomech. Model. Mechanobiol 10:599–611, 2011. [PubMed: 21058025]
35. Roccabianca S, Ateshian GA, and Humphrey JD. Biomechanical roles of medial pooling of glycosaminoglycans in thoracic aortic dissection. Biomech. Model. Mechanobiol 13:13–25, 2014. [PubMed: 23494585]
36. Sakalihasan N, Limet R, and Defawe O. Abdominal aortic aneurysm. Lancet 365:1577–1589, 2005. [PubMed: 15866312]

37. Shahmansouri N, Alreshidan M, Emmott A, Lachapelle K, Cartier R, Leask RL, and Mongrain R. Evaluating ascending aortic aneurysm tissue toughness: dependence on collagen and elastin contents. J. Mech. Behav. Biomed. Mater 64:262–271, 2016. [PubMed: 27526037]
38. Shimizu K, Mitchell RN, and Libby P. Inflammation and cellular immune responses in abdominal aortic aneurysms. Arterioscler. Thromb. Vasc. Biol 26:987–994, 2006. [PubMed: 16497993]
39. Sinha A, Shaporev A, Nosoudi N, Lei Y, Vertegel A, Lessner S, and Vyavahare N. Nanoparticle targeting to diseased vasculature for imaging and therapy. Nanomed. Nanotechnol. Biol. Med 10:e1003–e1012, 2014.
40. Vallabhaneni SR, Gilling-Smith GL, How TV, Carter SD, Brennan JA, and Harris PL. Heterogeneity of tensile strength and matrix metalloproteinase activity in the wall of abdominal aortic aneurysms. J. Endovasc. Ther 11:494–502, 2004. [PubMed: 15298501]
41. Vorp DA Biomechanics of abdominal aortic aneurysm. J. Biomech 40:1887–1902, 2007. [PubMed: 17254589]
42. Wang X, Lane BA, Eberth JF, Lessner SM, and Vyavahare NR. Gold nanoparticles that target degraded elastin improve imaging and rupture prediction in an AngII mediated mouse model of abdominal aortic aneurysm. Theranostics 9:4156–4167, 2019. [PubMed: 31281538]
43. Wilson JS, Bersi MR, Li G, and Humphrey JD. Correlation of wall microstructure and heterogeneous distributions of strain in evolving murine abdominal aortic aneurysms. Cardiovasc. Eng. Technol 8:193–204, 2017. [PubMed: 28378165]

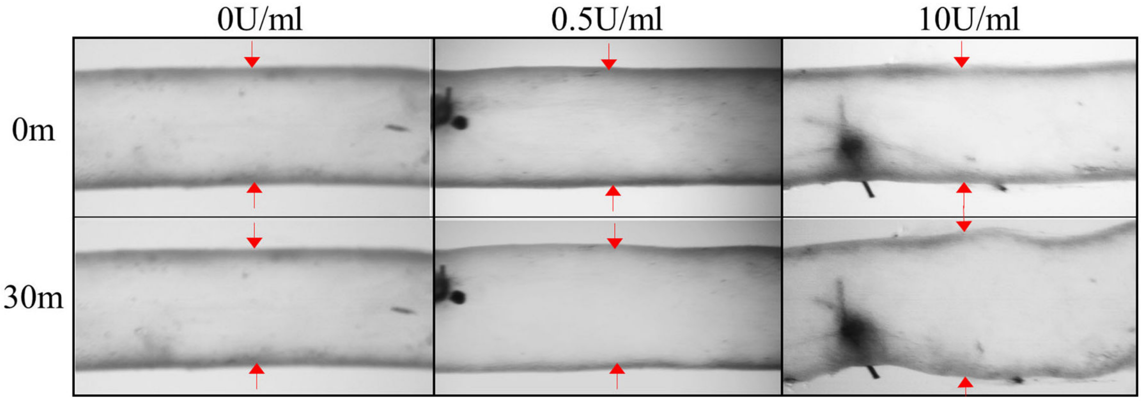

FIGURE 1.

Video micrographs of murine infrarenal aortas pre- and post-intraluminal perfusion of 0 (control), 0.5, and 10 U/mL of porcine pancreatic elastase for 30 min at 100 mmHg and *in vivo* axial stretches. Elastase treatment produced progressive elastin damage and dilation.

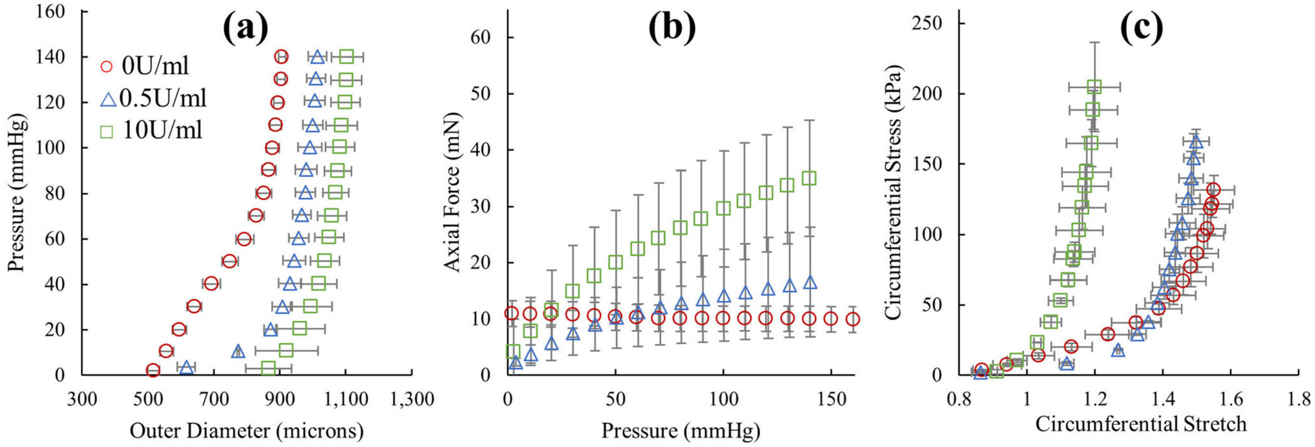

FIGURE 2.

Biaxial mechanical data illustrating the (a) pressure-diameter, (b) force-pressure, and (c) circumferential stretch-stress behavior of murine infrarenal aortas exposed to 0 U/mL (control; red circles), 0.5 U/mL (blue triangles), or 10 U/mL (green squares) of porcine pancreatic elastase. Data is shown at axial stretch ratios of 1.62 and 1.2 for the control and elastase-exposed groups, respectively. All data is presented as mean values ± the standard deviation (*n* = 4 per group) with pressure error-bars (roughly ± 0.45 mmHg) omitted for clarity.

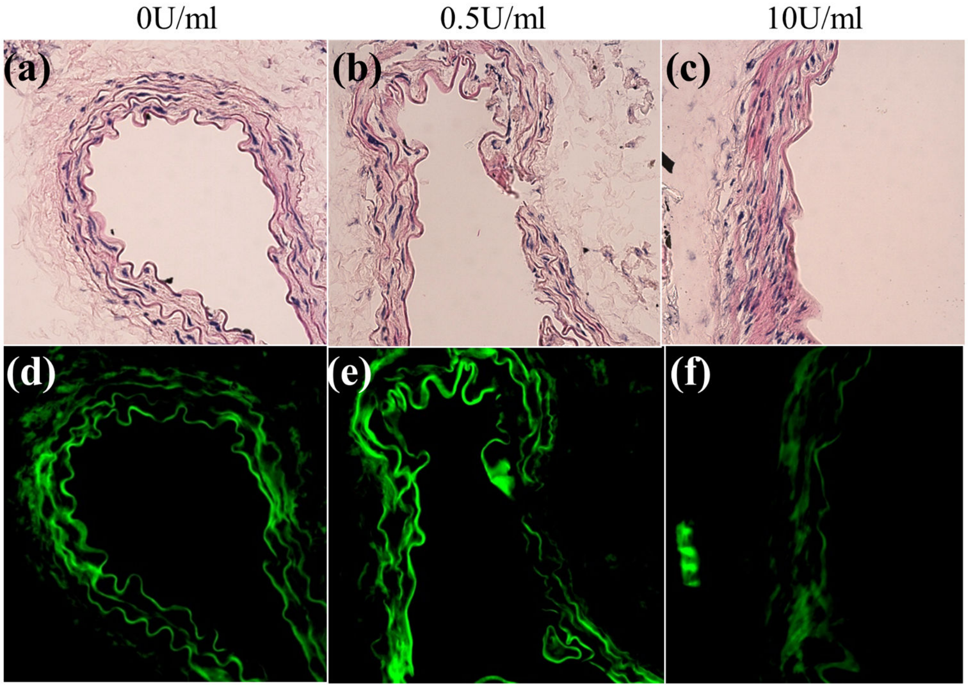

FIGURE 3.

Brightfield and fluorescence microscopy of murine infrarenal aortas following intraluminal perfusion of 0 (control), 0.5, and 10 U/mL of porcine pancreatic elastase for 30 min. (a-c) Hematoxylin and Eosin (H&E), (d-f) elastin autofluorescence.

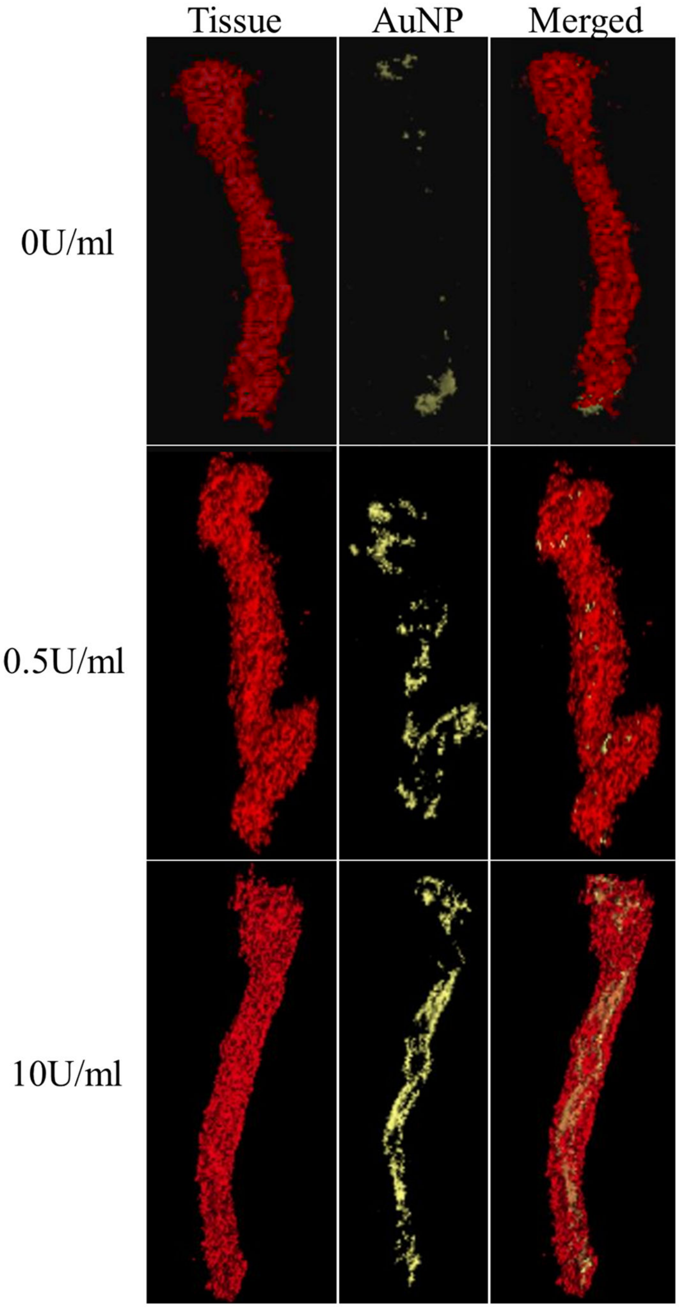

FIGURE 4.

Representative micro-CT scans after tissue and AuNP filtering to show (top) 0 U/mL control, (middle) 0.5 U/mL, and (bottom) 10 U/mL porcine pancreatic elastase-perfused infrarenal aortas after overnight incubation in elastin fragment-targeting EL-AuNP solution. All vessels are shown in the unloaded state after biaxial mechanical testing.

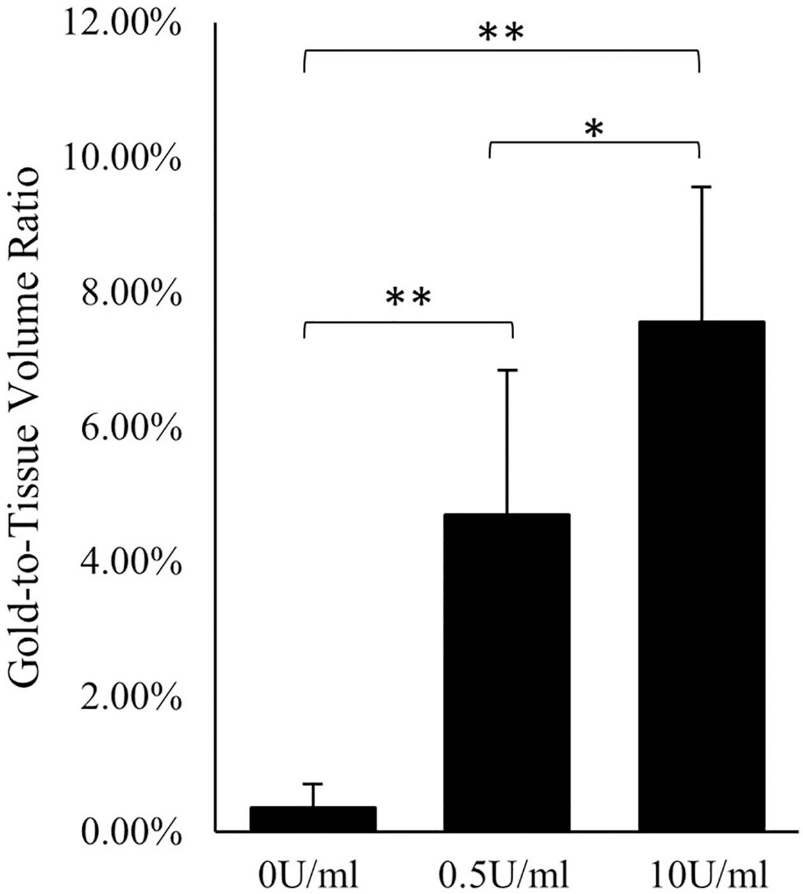

FIGURE 5.

Gold-to-Tissue volume ratios measured using micro-CT for 0 U/mL (control), 0.5 U/mL, and 10 U/mL of porcine pancreatic elastase perfused infrarenal aortas. (*) denotes p-val < 0.10 and (**) p-val < 0.05.

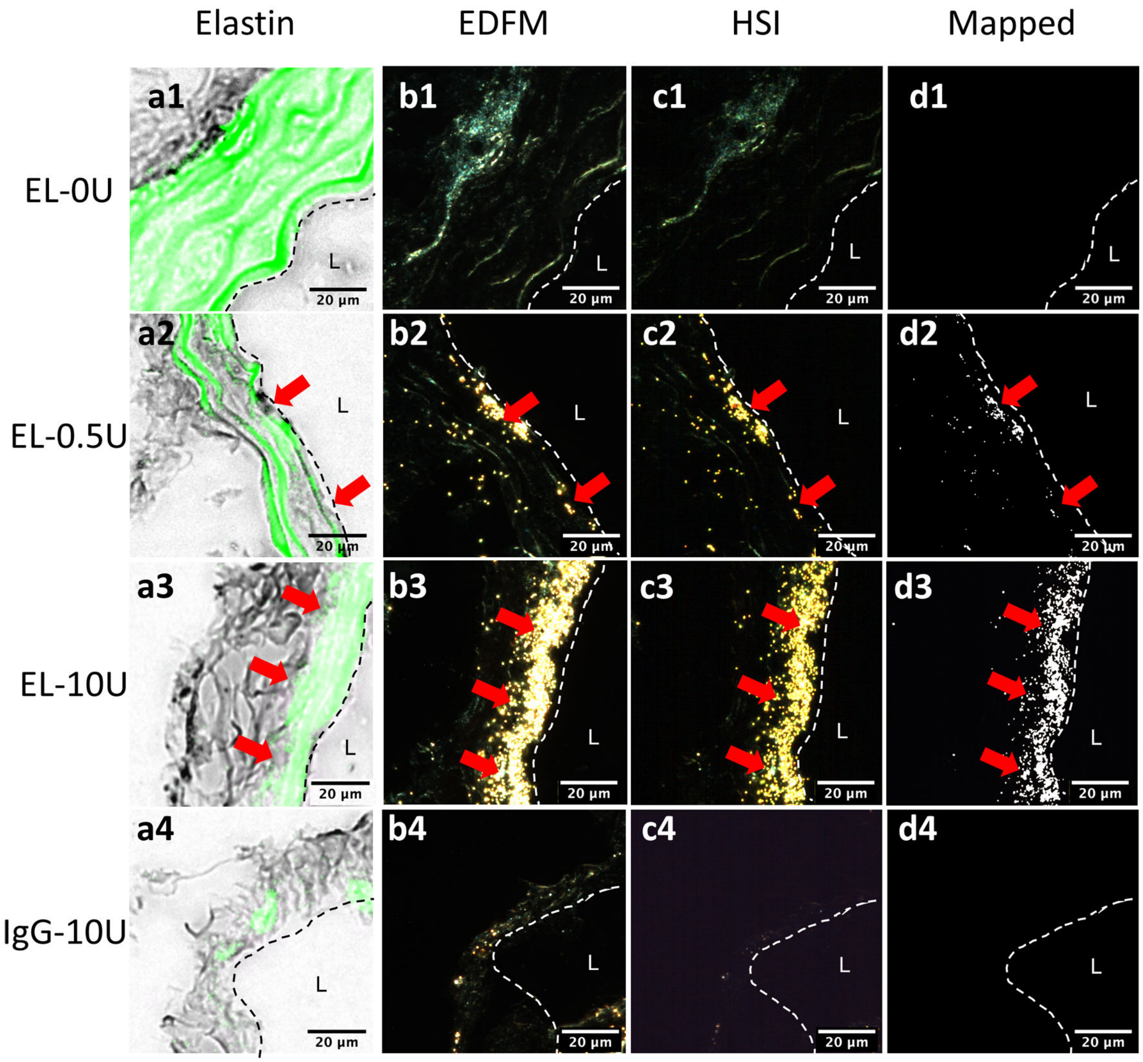

FIGURE 6.

Hyperspectral mapping of AuNPs in the infrarenal aorta at the site of elastin damage using (a) elastin autofluorescence, (b) enhanced darkfield microscopy, (c) hyperspectral imaging, and (d) the AuNP mapping for (1) 0 U/mL, (2) 0.5 U/mL, and (3) 10 U/mL elastase infused groups incubated with EL-AuNPs. Additionally, a separate 10 U/mL elastase infused aorta incubated with the non-reactive IgG-AuNPs (4) is shown. Dashed lines indicate the intimal layer to the lumen (L) with red arrows indicating regions of increased AuNP signal in darkfield imaging modes.

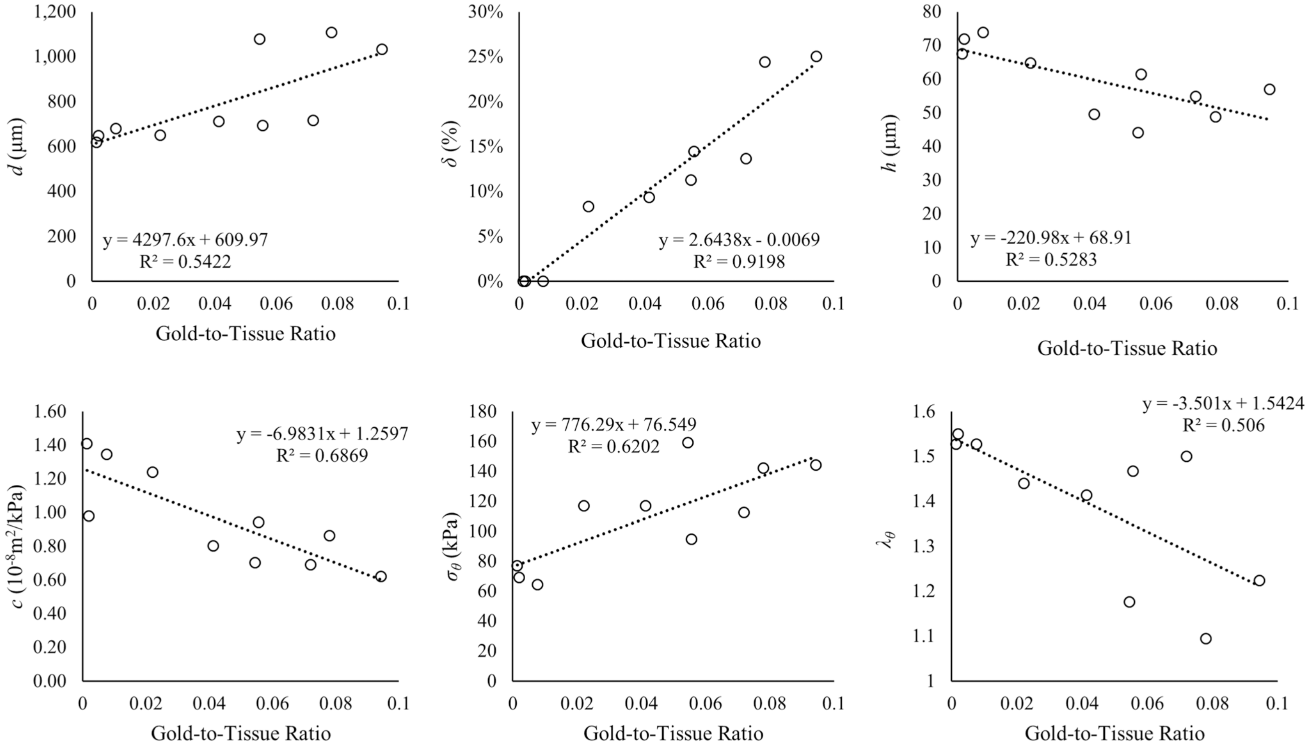

FIGURE 7.

Strong positive- and negative-trending relationships for biaxial (a-c) geometric and (d-f) mechanical parameters vs. Gold-to-Tissue volume ratios shown to be significant using Spearman's rank-order statistical analysis and ordinary least squares (OLS) linear regressions.

TABLE 1.

Biaxial geometric and mechanical metrics of loaded and unloaded murine infrarenal aortas following intraluminal perfusion at 0 U/mL (control), 0.5 U/mL, or 10 U/mL of porcine pancreatic elastase for 30 min.

	0 U/mL	0.5 U/mL	10 U/mL
D (μm)	649.5 ± 31.1	675.2 ± 29.6**	949.6 ± 76.0*^
H (μm)	112.9 ± 14.2	67.29 ± 1.92**	64.01 ± 5.70**
Λ (%)	–	1.59 ± 0.05	1.66 ± 0.07
δ (%)	–	12.0 ± 3.0	24.0 ± 1.0^
d (μm)	861.1 ± 28.4	992.0 ± 35.7**	1084 ± 44.2**^
h (μm)	71.14 ± 3.26	55.30 ± 5.95**	49.68 ± 6.66**
f (mN)	10.37 ± 1.1	12.96 ± 7.77	22.63 ± 0.66**^
c (10^{-8} m^2/kPa)	1.24 ± 0.23	0.98 ± 0.32	0.84 ± 0.21*
λ_θ	1.5 ± 0.04	1.45 ± 0.03**	1.17 ± 0.06**^
σ_θ (kPa)	70.24 ± 6.36	108.2 ± 11.8**	134.5 ± 15.2**^
σ_z (kPa)	59.35 ± 4.14	92.27 ± 63.2	192.1 ± 96.7**

(**) and (*) denote statistical differences from the control at p-val < 0.10 and < 0.05 respectively, while (^) denotes differences between experimental groups at p-val < 0.05.

TABLE 2.

Summary of Spearman Rank and ordinary least squares (OLS) regression analysis to assess relationships between specified geometric and biaxial mechanical indices and Gold-to-Tissue volume ratios.

		Soearman's Rank		OLS Regression Statistics			
Parameter	**Symbol**	ρ	**p-value**	**slope**	**vertical-intercept**	**R^2**	**p-value**
Dilation (%)	δ	0.976^{**}	<0.001	2.640^{**}	−0.007	0.92	0.015
Loaded Outer Diameter (µm)	d	0.867^{**}	0.003	$4{,}298^{**}$	610.0	0.54	0.015
Unloaded Outer Diameter (µm)	D	0.830^{**}	0.005	3216.7^{**}	633.37	0.43	0.04
Circumferential Stress (kPa)	σ_θ	0.673^{**}	0.039	776.3^{**}	76.55	0.62	0.007
Axial Stress (kPa)	σ_z	0.552	0.104	1,412	53.64	0.97	0.062
Axial Force (mN)	f	0.455	0.190	126.8	9.648	0.37	0.063
Unloaded Axial Elongation (%)	Λ	0.107	0.839	0.246	1.601	0.08	0.862
Loaded Thickness (µm)	h	-0.673^{**}	0.039	-221.0^{**}	68.91	0.53	0.017
Unloaded Thickness (µm)	H	-0.697^{**}	0.0311	-544.87^{**}	103.5	0.61	0.008
Circumferential Stretch Ratio	λ_θ	-0.723^{**}	0.018	-3.501^{**}	1.542	0.51	0.02
Lumen Area Compliance (10^{-8}m^2/kPa)	C	-0.830^{**}	0.006	-6.983^{**}	1.260	0.69	0.003

$^{(**)}$indicates p-val < 0.05.